AUTOMATIC CLASSIFICATION OF TISSUES USING T1 AND T2 RELAXATION TIMES FROM PROSTATE MRI: A STEP TOWARDS GENERATION OF PET/MR ATTENUATION MAP

Jorge Zavala Bojorquez, Stéphanie Bricq, Paul M. Walker, Alain Lalande

LE2I (UMR CNRS 6306). UFR Sciences de la Santé, Université de Bourgogne. 21079 Dijon, France.

ABSTRACT

This paper presents a new methodology providing the first step towards generating attenuation maps for PET/MR systems based solely on MR information. The new method segments and classifies the attenuation-differing regions of the patient's pelvis based on acquired T_1- and T_2-weighted MR data sets and anatomical-based knowledge by computing the tissue specific T_1 and T_2 relaxation times, using a robust implementation of the weighted fuzzy C-means algorithm and applying a novel process to detect bones. We have demonstrated the feasibility of this approach by correctly segmenting and classifying six differing regions of structural and anatomical importance: fat, muscle, prostate, air, background and bones.

Index Terms— MRI, attenuation, correction, T_1 and T_2 relaxation times, prostate, classification.

1. INTRODUCTION

Prostate cancer is the most commonly diagnosed cancer in men and a leading cause of cancer death worldwide [1]. To visualize, diagnose and evaluate prostate cancer, MRI is currently the imaging modality of choice due to its high tissue contrast, high resolution and ability to simultaneously image functional parameters. However, on the MR images, it is relatively difficult to detect cancer spread to the lymph nodes and the bones. Positron Emission Tomography / Computer Tomography (PET/CT) is considered as the gold standard to this end, but with the arrival of hybrid PET/MR systems and the advantages that MR represents with respect to CT, this is likely to change in the near future [2]. Nevertheless, the change cannot take place if an accurate method to generate the photon attenuation maps (μmaps), used for the reconstruction of PET images from MR information, is not designed. Different methods have been developed [3] [4] [5], but we will focus on voxel-based methods which attempt to derive the μmaps based on local information alone [5]. Unfortunately, there is no simple relation between MR image intensity and attenuation coefficients (ACs) [6]. Therefore, techniques applying a direct-mapping based on histogram matching produce μmaps with serious artefacts [7]. Thus, a natural extension of voxel-based methods is the intermediate step of image segmentation and classification [5], where ACs are assigned to the different image compartments [6]. These methods can be divided into two categories: the ones using spin-echo based sequences and those using special sequences. Methods using spin-echo based sequences to acquire proton density, T_1- and T_2-weighted MR images present one particular downside; signal intensities do not have any direct correspondence with the attenuation coefficients of the corresponding tissues. Moreover, the lack of image intensity standardization results in different transformation from tissue properties to image intensities [8]; the result is that the distribution of image intensities changes considerably from scan to scan [9] and the methods become scanner dependent. On the other hand, even if methods using special sequences bring in a meaningful signal from tissues producing no signal with conventional sequences (such as cortical bone), special sequences are not available in most of the commercial scanners and their implementation requires not only software updates, but mayor hardware modifications. To the best of our knowledge, most of these studies have been applied in brain and thorax imaging [3] [4] [5] and little efforts have been made to create accurate attenuation maps for prostate imaging. We propose a robust and automatic method based on the intrinsic parameters T_1- and T_2-relaxation times of tissues and anatomical knowledge to create accurate attenuation maps at the level of the pelvis with six regions: fat, muscle, prostate, air, background and bones. Our method does not require special sequences to extract bones neither does it depend on voxel intensities. Therefore, it is scanner independent and can be implemented on any system.

2. METHODOLOGY

In order to carry out the segmentation and classification of the different tissues present in an image, the developed approach exploits the information obtained from different standard MRI sequences. The sequences are used to obtain T1-weighted and T2-weighted images in order to compute the T_1 and T_2 maps. These maps serve as the input of the algorithm used for segmentation. Finally, the regions of the segmented

Contact: Jorge-Arturo.Zavala-Bojorquez@u-bourgogne.fr

image are compared with a priori knowledge to perform classification. The final image contains the labels and boundaries of the various tissues within.

2.1. Image Acquisition

The images were acquired with a 3T Trio TIM clinical scanner (Siemens Medical Solutions, Germany) using a phased array body coil. Two healthy volunteers (22 and 42 years old) had given their informed consent to participate in the study, which had been approved by the local institutional review board. Four axial slices were acquired for both T_1 and T_2 measurements with the same field of view (FOV), resolution and position at the level of the pelvis in order to avoid registration between T_1 and T_2 relaxation maps (Fig.1).

2.2. T1 Measurement

An inversion recovery-prepared turbo spin echo (TSE) was acquired at eight inversion times (TI) : 50, 200, 400, 700, 1200, 2000, 5000, 7860 ms to obtain the T1-weighted images. The TI were chosen to assure maximum contrast among tissues and to cover the whole span of T_1 relaxation times of tissues present in the slice section: muscle (1412 ms), fat (382 ms) and prostate (1597 ms) [10] [11]. Other parameters were: repetition time ($TR = 16000$ ms), echo time ($TE = 7.7$ ms), echo train length ($ETL = 7$), FOV (252 x 384 mm), number of excitation ($NEX = 1$), size of matrix (168 x 256), dimension of voxels (1.5 x 1.5 x 10 mm^3) and a resolution of 0.667 pixels/mm. The longitudinal relaxation time, T_1, was calculated from a magnitude monoexponential fit (Eq. (1)) to the signal recovery data for each voxel using the bisquare nonlinear least squares fitting method implemented in-house in Matlab (The Mathworks, Natick, MA. Version 2012b) scripts. A three-parameter model was used, with T_1, the equilibrium magnetization (S_o) and the inversion efficiency (α) included as variable fitting parameters:

$$S(TI) = |S_o(1 - \alpha e^{-TI/T_1})| \quad (1)$$

The use of a long TR ($> 5T_1$ of the longest T_1 of the tissues) allowed the fit to Eq. (1), since the longitudinal magnetization fully recovers before another repetition of the sequence is applied [12]. The fit was computed with the absolute values of Eq. (1) because these particular sequences provide magnitude images. To eliminate the influence of noise during the fit, the algorithm reduces the weight of outliers using bisquare weights and keeps fits with a good of fitness (R_{square}) of at least 0.85 (R_{square} values representing accurately $\geq 85\%$ of the measures).

To minimize the fitting time, the algorithm automatically extracts the background from the images and only fits to the region of the body. This is achieved by creating a binary image from the longest TI image with a threshold of 4% of the highest voxel intensity (at this TI the tissues have recovered

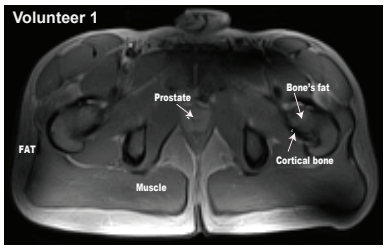

Fig. 1. Example of a T1-weighted axial slice at the level of the pelvis.

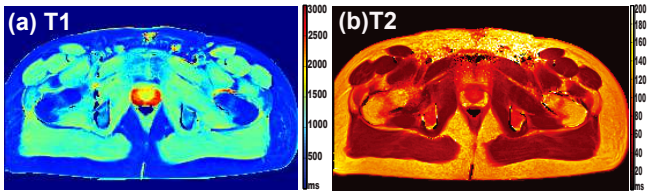

Fig. 2. T_1 and T_2 maps for volunteer 2.

their longitudinal magnetization and their intensity is maximum) and by keeping the region with the highest number of voxels. Likewise, the fitting time was reduced by setting the lower ($S_{o_l} = 1$, $\alpha_l = 1$, $T_{1_l} = 0.5$) and the upper ($S_{o_u} = 50000$, $\alpha_u = 2$, $T_{1_u} = 3000$) constraints of coefficients. Fig. 2a shows the calculated T_1 map.

2.3. T2 Measurement

The transverse relaxation time T_2 was measured using a 32-echo spin echo sequence acquired with TE from 8.8 to 281.6 ms in 8.8 ms steps and with a TR of 5000 ms. The same values for FOV, NEX, matrix size and voxel's dimension were defined as the T_1 acquisition. A monoexponential fit using again the bisquare nonlinear least squares fitting method was applied to the data. A three parameter model (Eq. (2)) was used with T_2, S_o and the y-offset (C) as fitting parameters:

$$S(TE) = S_o e^{TE/T_2} + C \quad (2)$$

The fit was calculated only in voxels belonging to the region of the body defined during the T_1 processing. The fits of voxels with $R_{square} \geq 85\%$ were kept. The bound constraints coefficients were set as follows: the lower $S_{o_l} = 1$, $T_{2_l} = 0.5$, $C_l = 1$ and the upper $S_{o_u} = 5000$, $T_{2_u} = 3500$, $C_u = 5000$. Fig. 2b shows the computed T_2 map.

2.4. Segmentation

Segmentation was performed using Weighted Fuzzy C-means (wFCM). We chose this algorithm among the variations of FCM [13] [14] [15] because it allows to bias the segmentation according to the weights chosen by the designer. In our case, the similarities are the T_1 and T_2 values of the different

Data: X,c,m,w
Result: U,V
while $max_{1\leq i\leq c}\{\|V_{i.new} - V_{i,old}\|^2\} > \epsilon$ **do**
Calculate U;

$$u_{i,j} = \left[\sum_{k=1}^{c}\left(\frac{\|x_j - v_i\|}{\|x_j - v_k\|}\right)^{\frac{2}{m-1}}\right]^{-1}, \forall i,j \quad (3)$$

Calculate V;

$$v_i = \frac{\sum_{j=1}^{n} w_j (u_{ij})^m x_j}{\sum_{j=1}^{n} w_j (u_{ij})^m}, \forall i \quad (4)$$

end

Algorithm 1: Weighted-FCM [16].

tissues. The voxels are assigned to one specific cluster taking into account their T_1 and T_2 relaxation times and its spatial relationship with the surrounding pixels. Both values are required because some tissues have very similar T_1 or T_2 times making their segmentation and their classification particularly difficult without this information.

The method performs a *fuzzy* partition where each of the data points (n) belongs to a cluster to some degree (See Algorithm 1). It takes as inputs the T_1 and T_2 maps represented by $X = x_{T1_1T2_1}, x_{T1_2T2_2}, ..., x_{T1_nT2_n}$, the number of clusters desired in the image $(2 \leq c \leq n)$, the fuzzification constant $(m = 2$, a standard value in the literature [13] [14]) which controls the fuzziness of the resulting partition, the weights that define the influence of each data in the clustering solution (w). In order to define the weighted vector, a common measure of the characteristics between the spatial information from T_1 map to T_2 map had to be designed. For example, a distance component and a special parameter to alter the contribution of T_1 and T_2 values are implemented in [17], to bias the segmentation towards those elements with the smallest values. The adopted measure here was entropy, to take advantage of the good spatial resolution of MR images, and because it allows to estimate the randomness of the information which is a common reference in both maps. It was computed for neighborhoods of 9x9 voxels from T_1 and T_2 maps, the weighted vector was formed by the inverse of the product of these values. The smaller the product the better the certainty about the measures. The centers of clusters were biased towards these measures (Eq. (5)):

$$\widetilde{w}_{k_{T_1T_2}} = 1/\left(\left(-\sum_{k=1}^{K} p_{T_1}(T_{1k}) log p_{T_1}(T_{1k})\right)\left(-\sum_{k=1}^{K} p_{T_2}(T_{2k}) log p_{T2}(T_{2k})\right)\right) \quad (5)$$

where T represents the different measures T_1 or T_2 and p_T their probabilities.

The membership matrix (U), which was initialized randomly, represents the extent with which each measure is associated to every cluster. Then, $U = u_{i,j} \epsilon [0,1], i = 1,2,...,c$ where u_{ij} tells the degree to which element x_j belongs to cluster c_i. It is calculated with Eq. (3). The set of cluster centers is represented by V, $v = (v_1, v_2, ..., v_n)$ and the constrained optimization function is given by Eq. (6):

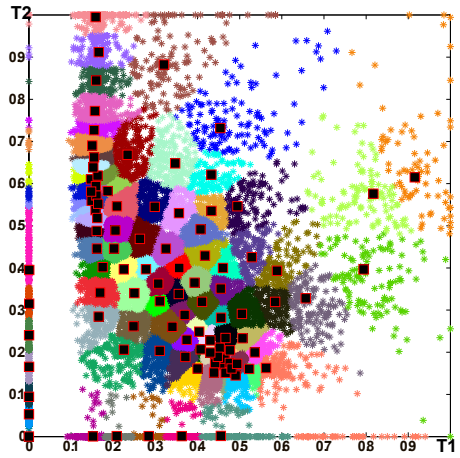

Fig. 3. Feature space of normalized T_1 and T_2 relaxation times. When tissues present similar T_1 values, the cluster's centroids (■) are defined according to their T_2 values and vice versa. The centroids are also biased towards relaxation times with the less entropy in their measures.

$$J_{mw}(U,V) = \sum_{i=1}^{c}\sum_{j=1}^{n} w_j u_{ij}^m \|x_j - v_i\|_A^2 \quad (6)$$

where $|A|$ can be any inner product A-induced norm $\Re^n$, and in this case it is the euclidean distance which has shown good results [16]. An over-segmentation of the image was chosen $(c = 100)$. Clusters are small and their centroid values represent more accurately the values of the cluster. T_1 and T_2 values were normalized to avoid bias towards T_1 values (T_1 >> T_2) . The resulting clusters can be seen in Fig. 3. The next step consists in assigning these clusters to specific tissues.

2.5. Classification

The classification process labels each cluster to its corresponding tissue. First, the centroid values of each cluster were compared with the references T_1 and T_2 values of the tissues using the euclidean norm (Eq. (7)):

$$d(ce, T_{ref}) = \sqrt{\left(ce_{T_1} - T_{1_{ref}}\right)^2 + \left(ce_{T_2} - T_{2_{ref}}\right)^2} \quad (7)$$

where ce represents T_1 and T_2 values of the centroids, T_{ref} are respectively those of the reference tissues. These reference values were calculated from the average values of different ROIs, set on the T_1 and T_2 maps of volunteer 1 for the following tissues: fat ($T_1 = 405 \pm 34ms$, $T_2 = 147 \pm 20ms$, $ROI = 1508$ voxels), muscle ($T_1 = 1290 \pm 83ms$, $T_2 =$

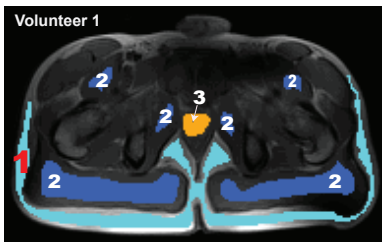

Fig. 4. The regions of interest set to obtain the reference T_1 and T_2 relaxation times drawn to maximize a region of homogeneous values: 1) fat, 2) muscle and 3) prostate.

$39 \pm 3ms$, $ROI = 1717$ voxels) and prostate ($T_1 = 1742 \pm 175ms$, $T_2 = 75 \pm 34ms$, $ROI = 125$ voxels) as shown in Fig. 4. For air, zero values were used for both T_1 and T_2 relaxation times. It was mandatory to compute these values, because there is a huge ambiguity over the values reported in the literature, where the relaxation times seem to vary according to the sequences and the methods used to calculate them [18]. The clusters were assigned to the tissue with which they have the smallest distance (Fig. 5a).

Secondly, it is well known that cortical bone does not produce signal with conventional spin echo sequences used in clinical practice [19]. Therefore, the use of T_1 and T_2 values is not enough to classify bones. For this reason, we introduced anatomical knowledge to detect and classify bones. The bones of the pelvis are composed of cortical bone and fat, the fat being surrounded by cortical bone, and the bone's regions having a symmetric counterpart on the opposite side of the image.

The approach consists of these steps: 1) From the previous segmented and classified image, the fat regions are localized (Fig. 5b); 2) A morphological opening operation is performed to remove small regions and narrow segments of fat connecting big regions (kernel size 3x3); 3) Regions in contact with the background are removed and regions having an area smaller than a predefined threshold (100 mm^2) are discarded (Fig. 5c); 4) For bones, the boundaries of the fat regions are surrounded by cortical bone, but since this tissue produces no signal with the implemented sequences, it is labeled as air. Therefore, the boundaries of the fat regions are localized (dilation, kernel size 5x5) and their labels analyzed. If the labels do not correspond to an area of at least 22.5 mm^2 of air, they are rejected; 5) Finally, symmetric regions are classified as bones (Fig. 5d) and potential miss-classified regions are re-evaluated with a step-by-step set of simple, but strong anatomical rules. The final classification can be seen in Fig. 5e.

3. RESULTS

Our method depends on the accurate calculation of the relaxation times T_1 and T_2. The obtained relaxation maps are homogeneous (Fig. 2), this shows that the fitting model correctly compensates for the inhomogeneities of the B_1-field yielding exact values. The cluster centroids obtained with the wFCM algorithm (Fig. 3) prove that the weighted-vector effectively biases the segmentation towards voxels presenting less randomness in their measures. A qualitative evaluation of the automatically achieved segmentation results was performed by an expert radiologist (Fig. 5e). The results were rated from good to excellent. Fat, muscle, prostate, air and background were correctly segmented and classified. Our results illustrate that classification of big bones is accurate. Nevertheless, small bone structures severely affected by partial volume effect were not detected.

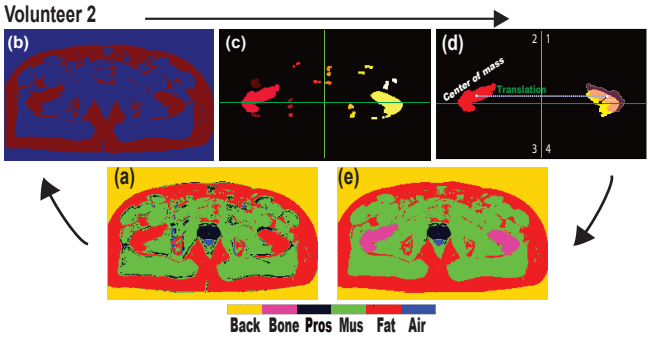

Fig. 5. The classification process. (a) Initial classification of tissues does not present bones, and a special process is implemented to detect them (b, c, d). (e) The final classification. See text for details.

4. CONCLUSIONS

In this work, we proposed a new methodology as a first step to generate the attenuation correction map of PET/MRI systems for prostate imaging. The approach utilizes standard MR sequences to segment and classify the tissues using the T_1 and T_2 relaxation times and anatomical-based knowledge. It correctly segments and classifies the attenuation-relevant structures used for this purpose: fat, air, background, bones and soft tissues. Furthermore, it sub-divides soft tissue into muscle and prostate and it does not rely on special sequences to segment and classify bones. However, further development will concentrate on the bone segmentation and classification procedure; thus, small regions of bones are affected by partial volume effect and cannot always be detected. The current results clearly demonstrate that the method could provide a first step to generate the attenuation map of PET/MRI systems in prostate imaging. The validation on a big data set is planned.

5. REFERENCES

[1] International Agency for Research on Cancer and Cancer Research UK, "World cancer factsheet," 2014.

[2] H. Herzog, "PET/MRI: Challenges, solutions and perspectives," *Zeitschrift für Medizinische Physik*, vol. 22, no. 4, pp. 281–298, 2012.

[3] G. Wagenknecht, H.-J. Kaiser, F. M. Mottaghy, and H. Herzog, "MRI for attenuation correction in PET: methods and challenges," *Magnetic Resonance Materials in Physics, Biology and Medicine*, vol. 26, no. 1, pp. 99–113, 2013.

[4] I. Bezrukov, F. Mantlik, H. Schmidt, B. Schölkopf, and B. J. Pichler, "MR-based PET attenuation correction for PET/MR imaging," *Seminars in Nuclear Medicine*, vol. 43, no. 1, pp. 45–59, 2013.

[5] V. Keereman, P. Mollet, Y. Berker, V. Schulz, and S. Vandenberghe, "Challenges and current methods for attenuation correction in PET/MR," *Magnetic Resonance Materials in Physics, Biology and Medicines*, vol. 26, no. 1, pp. 81–98, 2013.

[6] Y. Berker, J. Franke, A. Salomon, M. Palmowski, H. C. W. Donker, Y. Temur, F. M. Mottaghy, C. Kuhl, D. Izquierdo-Garcia, Z. A. Fayad, F. Kiessling, and V. Schulz, "MRI-based attenuation correction for hybrid PET/MRI systems: A 4-class tissue segmentation technique using a combined ultrashort-echo-time/dixon MRI sequence," *Journal of Nuclear Medicine*, vol. 53, no. 5, pp. 796–804, 2012.

[7] T. Beyer, M. Weigert, H. H. Quick, U. Pietrzyk, F. Vogt, C. Palm, G. Antoch, S. P. Müller, and A. Bockisch, "MR-based attenuation correction for torso-PET/MR imaging: pitfalls in mapping MR to CT data," *European Journal of Nuclear Medicine and Molecular Imaging*, vol. 35, no. 6, pp. 1142–1146, 2008.

[8] M. Hofmann, F. Steinke, V. Scheel, G. Charpiat, J. Farquhar, P. Aschoff, M. Brady, B. Schlkopf, and B.-J. Pichler, "MRI-based attenuation correction for PET/MRI: a novel approach combining pattern recognition and atlas registration," *Journal of Nuclear Medicine*, vol. 49, no. 11, pp. 1875–1883, 2008.

[9] J. E. Iglesias, I. Dinov, J. Singh, G. Tong, and Z. Tu, "Synthetic MRI signal standardization: application to multi-atlas analysis," *Medical image computing and computer-assisted intervention: MICCAI.*, vol. 13, no. 3, pp. 81–88, 2010.

[10] C. M. J. de Bazelaire, G. D. Duhamel, N. M. Rofsky, and D. C. Alsop, "MR imaging relaxation times of abdominal and pelvic tissues measured in vivo at 3.0 T: preliminary results," *Radiology*, vol. 230, no. 3, pp. 652–659, 2004.

[11] G. J. Stanisz, E. E. Odrobina, J. Pun, M. Escaravage, S. J. Graham, M. J. Bronskill, and R. M. Henkelman, "T1, T2 relaxation and magnetization transfer in tissue at 3T," *Magnetic resonance in medicine*, vol. 54, no. 3, pp. 507–512, 2005.

[12] P. A. Gowland and V. L. Stevenson, "T1: The longitudinal relaxation time," in *Quantitative MRI of the Brain*, Paul Tofts, Ed., pp. 111–141. John Wiley & Sons, Ltd, 2003.

[13] K.-S. Chuang, H.-L. Tzeng, S. Chen, J. Wu, and T.-J. Chen, "Fuzzy c-means clustering with spatial information for image segmentation," *Computerized Medical Imaging and Graphics*, vol. 30, no. 1, pp. 9–15, 2006.

[14] D. Selvathi and R. Dhivya, "Segmentation of tissues in MR images using modified spatial fuzzy c means algorithm," *2013 International Conference on Signal Processing Image Processing Pattern Recognition (ICSIPR)*, pp. 136–140, 2013.

[15] D.-C. Park, "Intuitive fuzzy c-means algorithm for MRI segmentation," *2010 International Conference on Information Science and Applications (ICISA)*, pp. 1–7, 2010.

[16] T.C. Havens, J.C. Bezdek, C. Leckie, L.O. Hall, and M. Palaniswami, "Fuzzy c-means algorithms for very large data," *IEEE Transactions on Fuzzy Systems*, vol. 20, no. 6, pp. 1130–1146, 2012.

[17] C. R. Traynor, G. J. Barker, W. R. Crum, S. C. R. Williams, and M. P. Richardson, "Segmentation of the thalamus in MRI based on T1 and T2," *NeuroImage*, vol. 56, no. 3, pp. 939–950, 2011.

[18] N. Stikov, M. Boudreau, I. R. Levesque, C. L. Tardif, J. K. Barral, and G. B. Pike, "On the accuracy of T1 mapping: Searching for common ground," *Magnetic Resonance in Medicine*, vol. 49, no. 2, pp. 514–522, 2014.

[19] I. L. H. Reichert, M. D. Robson, P. D. Gatehouse, T. He, K. E. Chappell, J. Holmes, S. Girgis, and G. M. Bydder, "Magnetic resonance imaging of cortical bone with ultrashort TE pulse sequences," *Magnetic Resonance Imaging*, vol. 23, no. 5, pp. 611–618, 2005.